5.2 Chemistry

5-2-1 Untangling the Mystery of Rewritable Optical Recording

Re-writable optical recording got its start in the 1960's with the suggestion of Ovshinsky of using the crystalline/amorphous phase transition in multi-element chalcogenide compounds [1]. Although IBM carried out promising early efforts in the 1970's, it was the work of Matsushita which culminated in the development of optical disks capable of more than a million re-write cycles [2]. Based upon these early developments, the 4.7 GB digital versatile disk random access memory (DVD-RAM) was successfully commercialized and is now the foundation of a major industry. A comprehensive search for the best phase change memory alloys in terms of performance and reliability resulted in the selection of $Ge_2Sb_2Te_5$ (DVD-RAM) and Ag-In-Sb-Te alloys (DVD-RW).

Recording in optical disks utilizes amorphous with higher reflectivity marks on a lower reflectivity poly-crystalline background. Amorphous regions are accomplished with a single laser with crystallized regions created by laser heating to a temperature just above the glass-transition temperature, while amorphous regions are generated using higher power, short laser pulses rapidly quench the $Ge_2Sb_2Te_5$ from temperatures above the melting point forming amorphous material. Minimum quench rate estimates range as high as 10^{12} K/s with switching times into the amorphous states on the order of nanoseconds [3], but until recently little was know about the details of the structural transition behind the process.

Starting with a structure determined by powder diffraction for the crystalline phase, we have used the XAFS technique to investigate the key local changes in local structure responsible for the unique properties. Rietveld fitting results indicated $Ge_2Sb_2Te_5$ crystallized in the rocksalt (Fm3m) structure with Ge/Sb on 4a and Te on the 4b site with (0.4/0.4) and 1.0 occupancy, respectively. Careful XAFS measurements at the K-edges of all three elements of the crystalline phase demonstrated the presence of three short and three long Ge–Te and Sb–Te bonds reminiscent of the bonding in the binary GeTe with the second nearest-neighbor Te–Te dis-
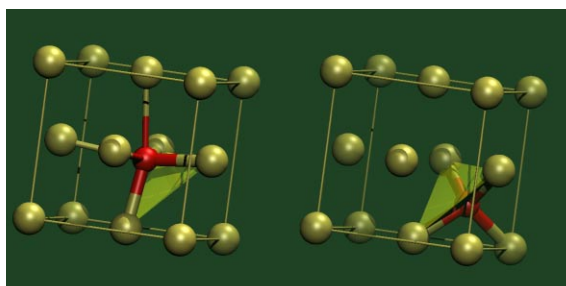
tances. Similar measurements clearly revealed an unusual increase in short-range order in moving from the crystalline to the amorphous phase. Ge–Te and Sb–Te bond lengths changed from 0.283 and 0.291 nm to 0.261 and 0.285 nm, respectively. The key mechanism behind the transformation is illustrated in Fig. 1 in which Ge atoms undergo a change in coordination from a distorted rocksalt like structure to their preferred tetrahedral coordination. The stochastic nature of the switch and the strengthening of short-range order induces relaxation of the Te unit cell destroying the long-range order. We refer to this transformation as "an umbrella" flip of Ge and is a result of the preferential breaking of the longer Sb–Te and Ge–Te bonds. It is this diffusion less transformation and the preservation of the Te sublattice (with some relaxation) that ensure that the transformation process is fast and reversible [4].

5-2-2 New Metastable Photo-induced Phase of Cu(II) Complexes

Photo-induced (PI) phase transitions have become an attractive subject in recent years relevant to the optical memory devices. It has been believed that the PI phase is the same state as the thermally induced high-temperature (HT) phase, however, Takahashi et al. [5] have reported a new type of the PI metastable phase in Cu(dieten)$_2$$X_2$ (dieten = N,N-diethylethylenediamine, X = BF$_4$ and ClO$_4$) complexes. These materials are known to exhibit thermochromic phase transitions; i.e., the low-temperature (LT) red phase consists of the planar CuN$_4$ unit and the CuN$_4$ unit is distorted tetrahedrally in the HT purple phase. Because the PI transition is expected to be similar to the thermally driven phase transition; the PI phase may contain the tetrahedrally distorted CuN$_4$ unit. The powder X-ray diffraction patterns of the PI phase were, however, found to be different from the HT phase, although no correspondence between the structure and diffraction patterns was deduced. The Cu K-edge XAFS spectra have been measured and analyzed to clarify the molecular structure in the PI phase [6]. The powdered thin sample was irradiated by UV light from an Hg lamp for 5–10 minutes at 30 K (see Experimental Setup in Fig. 2). Cu K-edge XANES spectra [Fig. 2(a)] show that the transition from 1s to 4pπ was found to be weakened and the spectral features at 8990 –9005 eV smeared out in both the thermally driven and photo-induced transitions, implying that the CuN$_4$ unit in the PI phase is distorted tetrahedrally, in a similar manner to the HT phase. In contrast, EXAFS spectra show a different finding in the second-nearest neighbor Cu–C shell [see Fig. 2(b)]. As shown in Fig. 2(c), the Fourier-filtered $\kappa^3\chi(\kappa)$ of the PI phase can be fitted much better by using the LT model. This implies that the configuration of the surrounding C atoms in the PI phase is closer to that of the LT phase. It is thus concluded that the PI phase is a new metastable state, whose intramolecular structure is not equivalent to that of either the HT or LT phase. The CuN$_4$ unit exhibits tetrahedral distortion,

while the atomic configuration of the ethylene and ethyl groups is similar to those of the LT phase. One can thus propose a possible model structure as shown in Fig. 3. The Cu(dieten)$_2$ ion has an inversion center in the LT phase (point group C_i) and a C_2 axis in the HT phase (point group C_2). When the LT phase is transformed to the PI phase by the UV irradiation, the CuN$_4$ plane is distorted tetrahedrally with less reconstruction of the dieten ligand than on the LT phase.

5-2-3 Dynamic Structure Changes during CO-Induced Disintegration of Surface Rh Clusters

Knowledge of the dynamic structure changes at the active site is important for the complete understanding of catalytic reactions. While the reaction mechanisms of molecules adsorbed on catalyst surfaces have been extensively studied, little is known about the dynamic structural change of active metal species in supported metal cluster/nanoparticle catalysts. The XAFS technique is the most suitable for the structural analysis of active sites under reaction conditions, and the in-situ method of time-resolved structural characterization using the dispersive XAFS (DXAFS) technique is essential for investigating dynamic properties on an atomic basis. The CO-induced disintegration process of Rh clusters on an Al$_2$O$_3$ surface have been successfully observed using the DXAFS technique [7], and the evaluated dynamic structure changes are summarized in Fig. 4.

Before the CO exposure, Rh atoms in the cluster interact with the surface oxygen of Al$_2$O$_3$ at the Rh–O distance of 0.213 nm, and the coordination number of the Rh–Rh interaction is 5.0 with the distance of 0.265 nm. These structural parameters suggest that the Rh cluster consists of 7 atoms (first layer) and 3 atoms (second
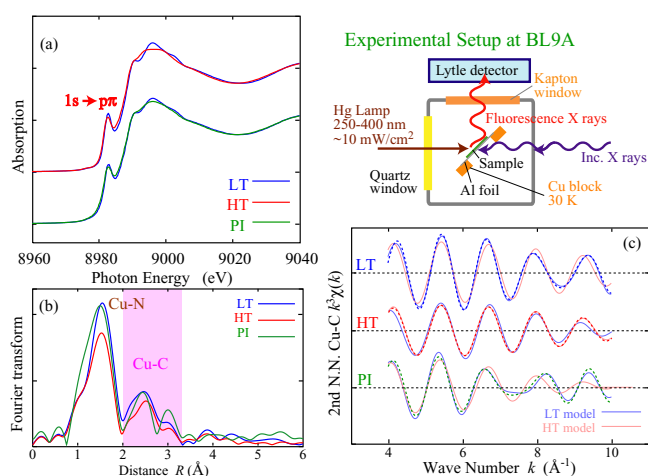

Figure 2
(a) Cu K-edge XANES spectra of the LT, HT and PI phases. (b) Fourier transforms of the EXAFS function $\kappa^3\chi(\kappa)$. (c) Fourier-filtered $\kappa^3\chi(\kappa)$ and the fitting results. These results are for the ClO$_4$ salt.
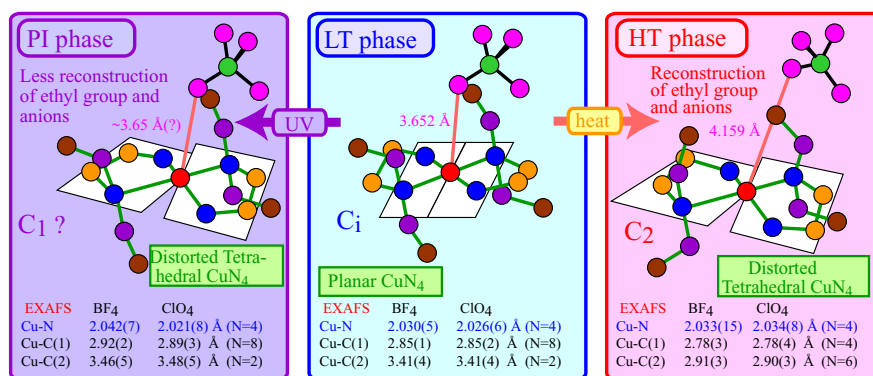

Figure 3
Proposed structure transformation in the photo-induced phase transition for the Cu(dieten)$_2X_2$ (dieten = *N,N*-diethylethylenediamine, X = BF$_4$ and ClO$_4$) complexes.
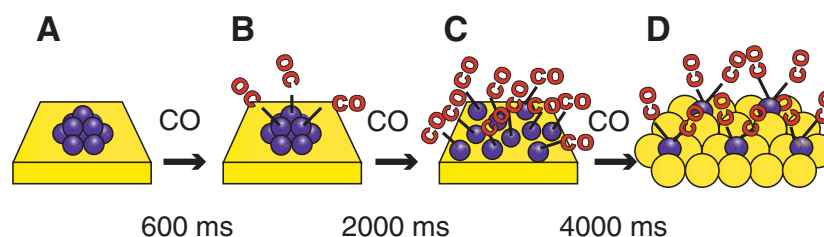

Figure 4
An evaluated mechanism showing time scales of the three elementary steps for the disintegration of Rh clusters on Al$_2$O$_3$ during CO adsorption at 298 K.

layer) as shown in Fig. 4(A). During the first step of the calbonylation (0–600 ms), the Rh clusters rapidly adsorb CO molecules, showing the coordination number of 0.7 for Rh–CO, indicating that one CO molecule adsorbs on each Rh atom of the top layer ($[Rh_{10}(CO)_3]$, Fig. 4(B)). No Rh–Rh bond breaking occurs at this stage, while it becomes weak due to the further CO adsorption at the second step after 600 ms. The Rh cluster is then completely disintegrated at 3000 ms, where the ratio of adsorbed CO to Rh reaches one ($[Rh-CO]_{10}$, Fig. 4(C)). The [Rh–CO] can migrate across the Al_2O_3 surface to react with OH groups. Fragmentation of the Rh cluster permits the adsorption of further CO molecules on the Rh atoms during the third step (3–6 s) to form $[Rh(CO)_2]$ (Fig. 4(D)) which interacts with three surface O atoms. The decrease in the Rh–O distance from 0.213 to 0.200 nm indicates that the Rh atoms interact more strongly with the surface at this process.

The time-resolved structural analysis provides crucial information for understanding the mechanism of dynamic surface processes and contributes to a new area of research into the structural dynamics of metal clusters/nanoparticles dispersed on surfaces.

5-2-4 Self-Assembly of Amphiphile Molecules

Self-assembly of amphiphile molecules is one of current key subjects in various research fields such as nano-scale technology, biotechnology, and molecular science. The ordering process of self-assembled monolayers (SAMs) of alkanethiolate, particularly on the (111) surface of gold, has been extensively studied as the simplest prototypical SAM system to understand the self-assembly mechanism [8]. It is widely known that the Au–thiolate interface structure on the Au(111) surface is similar to the hexagonal molecular lattice in the (001)

plane of single crystal bulk alkane, leading to facile formation of strain-free well-ordered monolayers. In case of Cu(100), however, there is an obvious difference in structure between the four-fold-symmetry surface and the molecular packing in the bulk alkane, which will cause significant lattice mismatch between the Cu–thiolate interface and the alkyl chain layer. Thus it is very intersting to elucidate how the alkanethiolate molecules reconcile the lattice mismatch to form the self-assembled monolayer, and it will be quite important to understand the self-assembly mechanism because this kind of situation is rather general for actual molecular self-assembling systems.

STM observations for a hexanethiolate monolayer adsorbed on Cu(100) revealed that the two dimensionally (2D) ordering process needs a much longer period (more than 10 hours) compared to that on Au(111). This enables us to trace the self-assembling process by using the surface XAFS technique [9]. Figure 5 shows Fourier transforms of S-K EXAFS oscillations for the hexanethiolate monolayer measured before (top) and after (bottom) the self-assembly. Quantitative analyses for S–Cu shells indicated that the sulfur atom of the thiolate is located at the four-fold hollow site of the unreconstructed Cu(100) surface irrespective of self-assembly. Although no drastic change was observed after self-assembly, it is appreciable that a new peak appears at around 0.32 nm, which is associated with the contribution from the nearest-neighbor (NN) sulfur atoms. The curve fitting analysis for this peak reveals that the NN sulfur atoms are located at the distance of c(2 × 2) lattice (S1 in the Inset). The absence of the peak at 0.32 nm before self-assembly implies poor ordering at the Cu–S interface, though C-K NEXAFS shows standing-up alignment of the alkyl chains even just after adsorption.
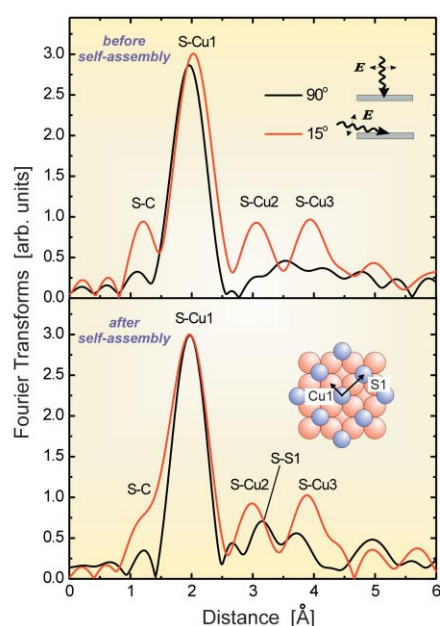

Figure 5
Fourier transforms of S-K EXAFS oscillation for a hexanethiolate monolayer on Cu(100) before (top) and after (bottom) self-assembly.
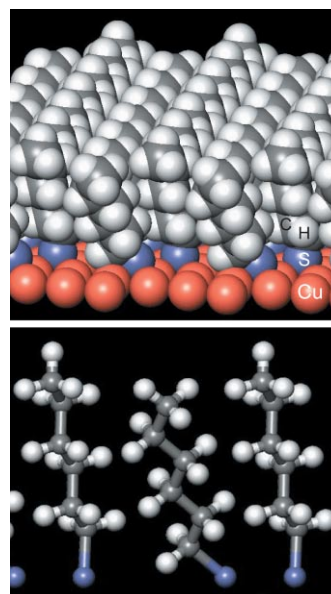

Figure 6
Structure model of hexanethiolate self-assembled monolayer on Cu(100) determined by combination of the XAFS results and the molecular force-field calculation in the bird's-eye view (top) and the side view (bottom).

Thus, surface thiolates rapidly form a well-aligned but 2D-disordered monolayer while randomly occupying the hollow sites. This rapid process is followed by slow evolution of the 2D-ordered structure via surface diffusion. Combination of the EXAFS results and force field calculations revealed that a large lattice mismatch between the S/Cu layer and the alkyl chain layer (31% max) is effectively reduced (7% max) by tilting half of the S–C bonds that bridges the two layers as shown in Fig. 6. The S–C bond tilting was detected as a decrease in the polarization dependence of the S–C contribution in S-K XAFS spectra after self-assembly. The XAFS study provides clear evidence for the self-assembly mechanism, in which the lattice mismatch is effectively accommodated by the internal degree of freedom of the molecule at the interface.

5-2-5 Charge-Discharge Mechanism of High Capacity Oxide-Anode-Materials for Li Secondary Battery

During the last three decades, enormous researches and developments have been undertaken to search available rechargeable battery system with more advanced performance than the lead-acid battery. These efforts were motivated by requirements for new power systems, e.g., portable computers, computer memory preservation, and mobile phones. Under these circumstances, an epoch-making novel battery system, the Li battery, was proposed, which has the high energy density and the high output potential. Commercially available Li ion batteries generally employ graphitized carbon as the anode material. However capacity is limited to about 370 A h kg^{-1} which is substantially smaller than that of metallic lithium, and rate properties are not enough for consideration as the anode for large-scale batteries. In order to overcome these problems, a novel anode material for a Li ion secondary battery, MnV_2O_6, was prepared [10] and characterized [11,12].

X-ray diffraction (XRD) analysis indicated that MnV_2O_6 has a brannerite type structure. Figure 7 shows the charge-discharge profiles of MnV_2O_6 at the first and
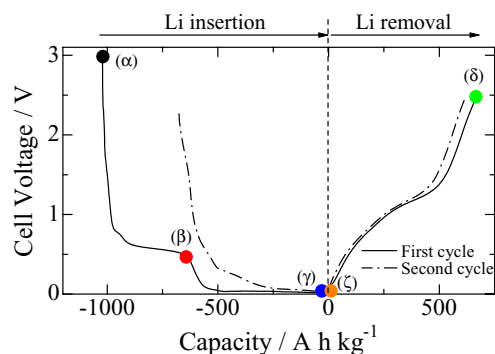
Figure 7.
The first and second charge-discharge curves of MnV_2O_6. Solid circles represent the cell voltage (α) before electrochemical measurement, (β) at 0.40 V during the charge process, (χ) at 0.01 V during the charge process, (δ) at 2.5 V during the discharge process, and, (ϵ) at 0.01 V during the second charge process.

second cycles [12]. Solid circles represent the voltages at which XAFS measurements of the electrodes were carried out. The profiles indicate that the first charge (Li insertion in MnV_2O_6) shows a large capacity of about 1000 A h kg^{-1}, which is much larger than that of graphite. Figure 8 shows the Fourier transforms of the Mn K-edge (a,b) and V K-edge (c,d) EXAFS spectra for the electrode at various potentials during the first Li insertion (a,c) and following extraction and reinsertion (b,d). In the case of the electrode before the electrochemical measurement shown in Fig. 8(a), the first peak located around 0.17 nm corresponds to the Mn–O interaction and the second one centered at 0.30 nm can be attributed to the Mn–Mn and/or the Mn–V interactions. The Fourier transforms for Mn and V indicate that the local structure reversibly changes during the cycles, even though the long range structure cannot be observed by XRD after the first charge. However, the local environments at 2.5 V during the discharge (δ) for both Mn and V in the active material differ from those in the MnV_2O_6 electrode before the electrochemical measurement (α). This phenomenon accounts for the irreversible capacity in the first cycle, which is observed in Fig. 7, because of the different lattice potentials between the electrode
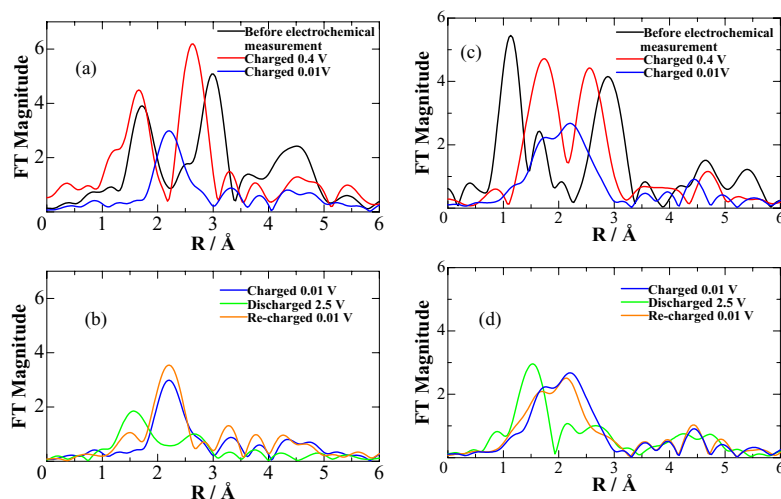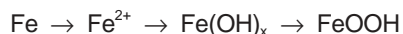
Figure 8
Fourier transforms of the Mn (a,b) and V (c,d) K-edge EXAFS spectra for the electrodes at various voltages. (a,c); the first charge, (b,d); following discharge and re-charge.

before the electrochemical measurement and at 2.5 V during discharge. It is thus concluded that controlling the local structure around the transition metals is an effective way of improving anode properties.

5-2-6 Corrosion Protection of Steel by "Protective Rusts"

Loss due to steel corrosion is estimated to be equivalent to more than a few percent of Japanese GNP. Steel used with no coating has a high demand not only due to its low costs but also from life-cycle assessment considerations for materials. The weathering steel (WS), containing 0.3–0.7 % of Cr and Cu, has been developed for the use in bridges without coating, and it forms a protective rust layer after a few years of corrosion under atmosphere and the amount of corrosion is 1/5 that of normal mild steel (MS). Macroscopic analysis has shown that the rust formed on WS is composed of fine grains, which can be attributed to a good corrosion resistance. However, there has been little information on the mechanisms of how the addition of a small amount of other elements results in the formation of "protective rusts". The formation of colloidal rusts at the early stage of corrosion is investigated using ex situ and in situ XAFS and the generalized grazing-incidence-angle X-ray scattering measurements [13,14]. It has been shown that the addition of even a small amount of elements changes drastically the initial process of corrosion: the nucleation of the $Fe(O,OH)_6$-network and its growth results in different morphology of the rusts grains (see Fig. 9). The anodic corrosion reaction is simply expressed by the next chemical equation.

$$Fe \rightarrow Fe^{2+} \rightarrow Fe(OH)_x \rightarrow FeOOH$$

When the reaction of rust formation is considered as the sum of the nucleation and the grain growth, the total rate of reaction (ν) can be written by the following equation,
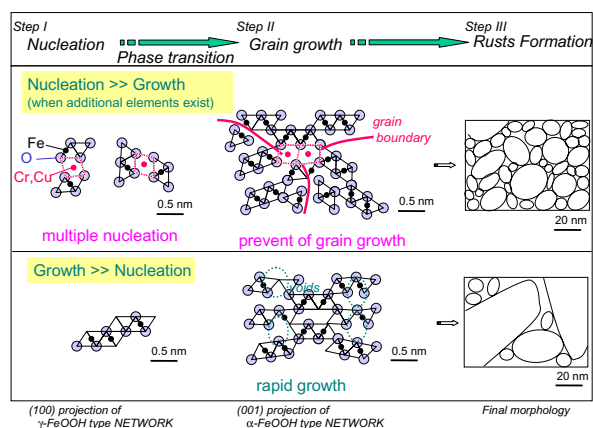
$$\nu = N \exp(-E_{Nucl} / kT) \exp(-E_{Growth} / kT)$$

where N is the number of reaction sites, and E_{Nucl} and E_{Growth} are the activation energies of nucleation and growth of the reaction products, respectively. At the initial stage of corrosion, the $Fe(O,OH)_6$ units nucleate from Fe^{2+}. Alloy elements such as Cr increase the atomic level heterogeneity in rusts by occupying different sites in the network, leading to an increase in N. It is also expected that the nucleation energy of the $Cr(O,OH)_6$ unit is lower than that of the Fe analogue, and thus that it decreases E_{Nucl}. The increase in N and the decrease in E_{Nucl} result in a situation where the rate of nucleation is larger than that of growth. This induces refinement of rust particles as small as a few nm (Fig. 9, top). In contrast, because the rate of corrosion (or growth) is large in MS, the reaction is nucleation-limited, and the rusts are considered to be composed of large grains containing many defects (Fig. 9, bottom). A new concept of corrosion is proposed as the evolution of the $Fe(O,OH)_6$-network. In order to understand its mechanism, in situ observation of the reaction at the interface between metal surfaces and liquid is important, and such studies are expected to lead us to designing a new type of WS.

5-2-7 Arsenic Behavior in Paddy Field

Recently, naturally occurring As contamination in ground water in the Ganges delta plain (Bangladesh and West Bengal in India) has been an important environmental issue. In such areas, ground water containing a large amount of As is not only used for drinking water but also widely used for irrigation for paddy fields. If the As in the soil is transported to rice grain, the risk of As poisoning can be larger for the people. The paddy field usually has a distinct cycle of flooded and non-flooded periods, where the redox conditions in the paddy soil change drastically during the cycle. The redox change should give a big impact on the behavior of As in water, soil, and plant system, because As can be readily dissolved from the solid phase and become mobile under the reducing conditions. However, the study on As behavior using the actual paddy field has not widely been examined.

The Eh (redox potential) variation for the paddy field showed that the value decreased after water was introduced to the field at the beginning of May, which continues during the flooded period until the end of August. The abundance profiles of As, Fe, and Mn in surface and soil water show that their concentrations were low under oxidative condition during the non-flooded period. In contrast, the dissolved concentrations of these ions increased under the reductive condition in the flooded period. This shows that the redox change induces the drastic change of the behavior of As related to the dissolution of Fe and Mn. Oxidation states of As, Fe, and Mn in soil were determined by the XANES spectroscopy [15,16]. For As, it was found that As(III) fraction in soil

Figure 9
Change of atomic structures of rusts during corrosion in WS (above) and MS (below). Additional elements change the process of $Fe(O,OH)_6$-network evolution, resulting in different morphologies of rust grains.

increased from 30 % in non-flooded period (April) to 70 % in flooded period (August) as shown in Fig. 10. The larger distribution coefficient of As(III) into aqueous phase compared with As(V) implies that the increase in As(III) proportion in soil can cause the increase in total As concentration in water. The increase of the As concentration coupled with the reduction of As(V) is also simulated by laboratory incubation experiments. The As(III)/As(V) ratio in soil measured by XANES showed that the ratio increased with time due to the development of reductive environment, while HPLC-ICP-MS analysis showed that As(III) is the dominant species in the aqueous phase. During the period, the total concentration of As in water phase increased with time. These results were similar to what was observed in the As behavior in the experimental paddy field. It is thus strongly suggested that the increase of As under the flooded condition is not only caused by the reductive dissolution of Fe oxide or hydroxide, but partly by the reduction of As(V) to As(III) due to the more mobile characteristic of As(III) than As(V). These results imply that rice grains likely incorporate As from soil water because the main growth of rice takes place during the flooded period.

5-2-8 Actinide Chemistry

Actinide chemistry contributes to the peaceful use of atomic energy techniques from the view point of the development of recycling methods of fissile materials from spent fuel and safety disposal methods of the radioactive wastes. Additionally, 5f electronic states in actinide compounds are attracting interest due to their intermediate natur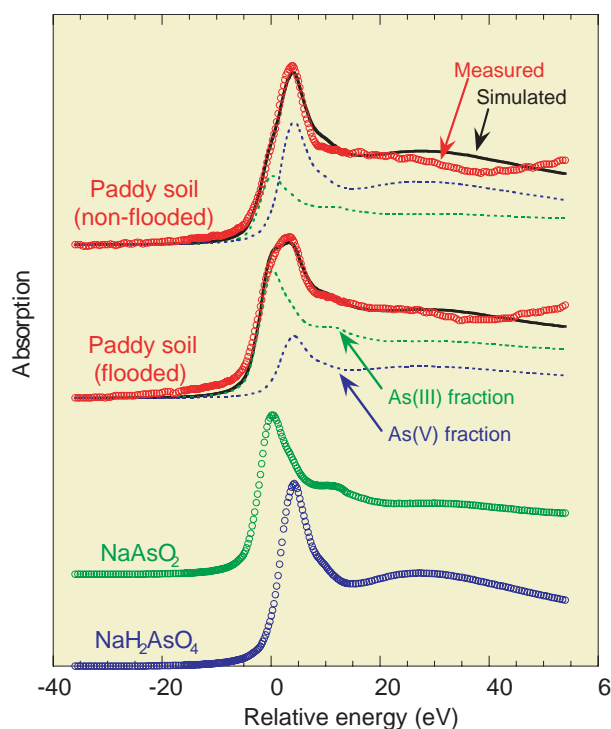e between rare earth 4f and transition metal 3d electrons from the viewpoint of fundamental chemistry. In order to clarify the unique electronic properties of actinides, the U-L_{III} XANES spectra of uranium metallofullerenes have been measured. The valence state of the encapsulated uranium has been estimated based on the chromatographic behavior of the metallofullerenes. The candidate structure of U@C_{82}, estimated from La@C_{82} [17], is shown in Fig. 11, in which the XANES spectra are shown for U@C_{82}, U_2@C_{80}, and some reference compounds. The edge energies of uranium were determined as the inflection point at the absorption edge estimated by the second derivative (solid lines in Fig.11). These energies are assigned to the transition from the $2p_{3/2}$ to the 6d state. The chemical shifts of UCl_3 and $UO_2(NO_3)_2 \cdot 2H_2O$ are ca. –5 eV and about 1.6 eV relative to UO_2, respectively. These differences are essentially the difference in the Coulomb interaction between the $2p_{3/2}$ core hole and the 5f electronic states of these compounds, and thus demonstrate the screening power of an additional 5f electron. The shift values of the uranium metallofullerences (U@C_{82} and U_2@C_{80}) are approximately equal to that of UCl_3, suggesting that the valence state of the uranium is +3 in the fullerences. On the basis of a general understanding of the uranium oxidation state, because the +3 state is stable only in the reducing conditions, it is thus concluded that the carbon cage corresponds to a very reducing condition.
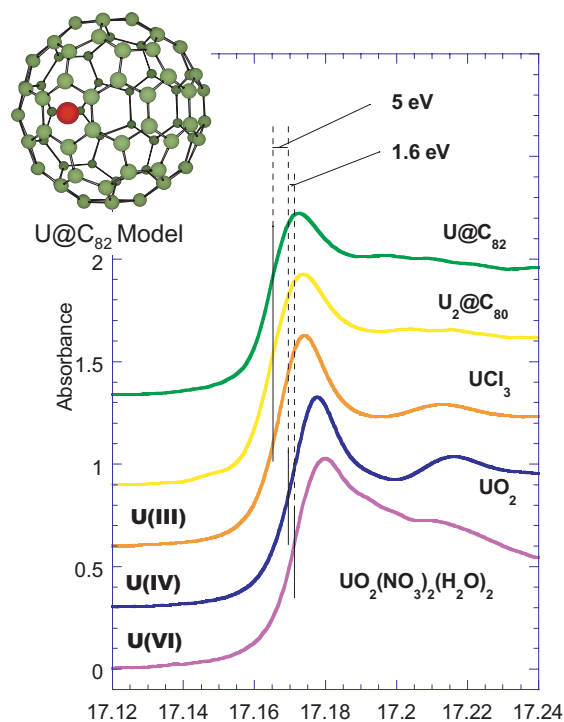

Figure 11
U-L_{III} XANES spectra of uranium metallofullerenes and reference compounds. The solid lines are the inflection points of the absorption edge, and the energy values are relative to that of UO_2. The illustration in the figure shows the candidate structure of U@C_{82}, estimated from La@C_{82}.

Figure 10
As K-edge XANES spectra of soil recovered under flooded and non-flooded conditions with those of $NaAsO_2$ and NaH_2AsO_4.

References

[1] S. R. Ovshinsky, *Phys. Rev. Lett.*, **21** (1968) 1450.

[2] T. Ohta, J. Optoelectron. *Adv. Mater.*, **3** (2001) 609.

[3] V. Weidenhof, N. Pirch, I. Friedrich, S. Siegler and M. Wuttig, *J. Appl. Phys.*, **88** (2000) 657.

[4] A. V. Kolobov, P. Fons, J.Tominaga, A. Frenkel, A. L. Ankudinov and T. Uruga *Nature Materials*, **3** (2004) 703.

[5] K. Takahashi, R. Nakajima, Z.-Z. Gu, H. Yoshiki, A. Fujishima and O. Sato, *Chem. Commun.* (2002) 1578.

[6] T. Yokoyama, K. Takahashi and O. Sato, *Phys. Rev. B* **67** (2003) 172104.

[7] A. Suzuki, Y. Inada, A. Yamaguchi, T. Chihara, M. Yuasa, M. Nomura, and Y. Iwasawa, *Angew. Chem. Int. Ed.*, **42** (2003) 4795.

[8] H. Kondoh, C. Kodama, H. Sumida and H. Nozoye, *J. Chem. Phys.* **111** (1999) 1175.

[9] H. Kondoh, N. Saito, F. Matsui, T. Yokoyama, T. Ohta and H. Kuroda, *J. Phys. Chem. B* **105** (2001) 12870.

[10] D. Hara, H. Ikuta, Y. Uchimoto and M. Wakihara, *J. Mater. Chem.* **12** (2002) 2507.

[11] D. Hara, J. Shirakawa, H. Ikuta, Y. Uchimoto, M. Wakihara, T. Miyanaga and I. Watanabe, *J. Mater. Chem*. **13** (2003) 897.

[12] D. Hara, J. Shirakawa, H. Ikuta, Y. Uchimoto, M. Wakihara, T. Miyanaga and I. Watanabe, *J. Mater. Chem.* **12** (2002) 3717.

[13] M. Kimura, T. Suzuki, G. Sigesato, M. Saito, S. Suzuki, H. Kihira, K.Tanabe and Y. Waseda, *J. Japan Inst. Metals* **66** (2002) 166.

[14] M. Kimura, A. Acosta, H. Fujioka, and M. Oshima, *J. Appl. Phys.* **93** (2003) 2034.

[15] Y. Takahashi, R. Minamikawa, K. H. Hattori, K. Kurishima, N. Kihou and K. Yuita, *Environ. Sci. Technol.*, **38** (2004) 1038.

[16] Y. Takahashi, N. Ohtaku, S. Mitsunobu, K. Yuita and M. Nomura, *Anal. Sci.*, **19** (2003) 891.

[17] H. Suematsu et al., Mat. Res. *Soc. Symp. Proc.*, **349** (1994) 213.